APPLIED OPTICS

Photonic spin-controlled multifunctional shared-aperture antenna array

Elhanan Maguid,[1]* Igor Yulevich,[1]* Dekel Veksler,[1]* Vladimir Kleiner,[1] Mark L. Brongersma,[2] Erez Hasman[1]†

The shared-aperture phased antenna array developed in the field of radar applications is a promising approach for increased functionality in photonics. The alliance between the shared-aperture concepts and the geometric phase phenomenon arising from spin-orbit interaction provides a route to implement photonic spin-control multifunctional metasurfaces. We adopted a thinning technique within the shared-aperture synthesis and investigated interleaved sparse nanoantenna matrices and the spin-enabled asymmetric harmonic response to achieve helicity-controlled multiple structured wavefronts such as vortex beams carrying orbital angular momentum. We used multiplexed geometric phase profiles to simultaneously measure spectrum characteristics and the polarization state of light, enabling integrated on-chip spectropolarimetric analysis. The shared-aperture metasurface platform opens a pathway to novel types of nanophotonic functionality.

Multifunctional planar systems that can perform a number of concurrent tasks in a shared aperture were recently introduced in the field of phased-array antennas for radar applications. In particular, modern radio frequency sensing, communication, and imaging systems based on sparse phased-array antennas are able to operate at different frequency bands, polarizations, scanning directions, etc. These capabilities are ascribed to subarrays of elementary radiators, sharing a common physical area that constitutes the complete aperture of the phased array (*1*–*4*). The shared-aperture concept can be adopted to realize multifunctional photonic antenna arrays. The recent implementation of metasurfaces, or metamaterials of reduced dimensionality, is of particular relevance, as it opens up new opportunities to acquire virtually flat optics. Metasurfaces consist of a dense arrangement of resonant optical antennas on a scale smaller than the wavelength of external stimuli (*5*–*10*). The resonant nature of the light-matter interaction of an individual nanoantenna affords substantial control over the local light scattering properties. Specifically, the local phase pickup can be manipulated by tailoring the antenna material, size, and shape, as well as environment–antenna resonance shaping (*11*–*15*), or through the geometric phase concept (*10*, *16*–*20*). The latter concept is an efficient approach for achieving spin-controlled phase modulation, whereas the photon spin is associated with the intrinsic angular momentum of light (*21*). Such a geometric phase metasurface (GPM) transforms an incident circularly polarized light into a beam of opposite helicity, imprinted with a geometric phase $\phi_g(x, y) = 2\sigma_\pm\theta(x, y)$, where $\sigma_\pm = \pm 1$ denotes the polarization helicity [photon spin in $\hbar$ units ($\hbar$ is Planck's constant h divided by 2π)] of the incident light, and $\theta(x, y)$ is the nanoantenna orientation (*22*). Here we incorporate the shared-aperture phased antenna array concept and spin-controlled two-dimensional (2D) optics based on nanoantennas. By use of the geometric phase mechanism, the

[1]Micro and Nanooptics Laboratory, Faculty of Mechanical Engineering, and Russell Berrie Nanotechnology Institute, Technion – Israel Institute of Technology, Haifa 32000, Israel. [2]Geballe Laboratory for Advanced Materials, Stanford University, 476 Lomita Mall, Stanford, CA 94305, USA.
*These authors contributed equally to this work. †Corresponding author. Email: mehasman@technion.ac.il

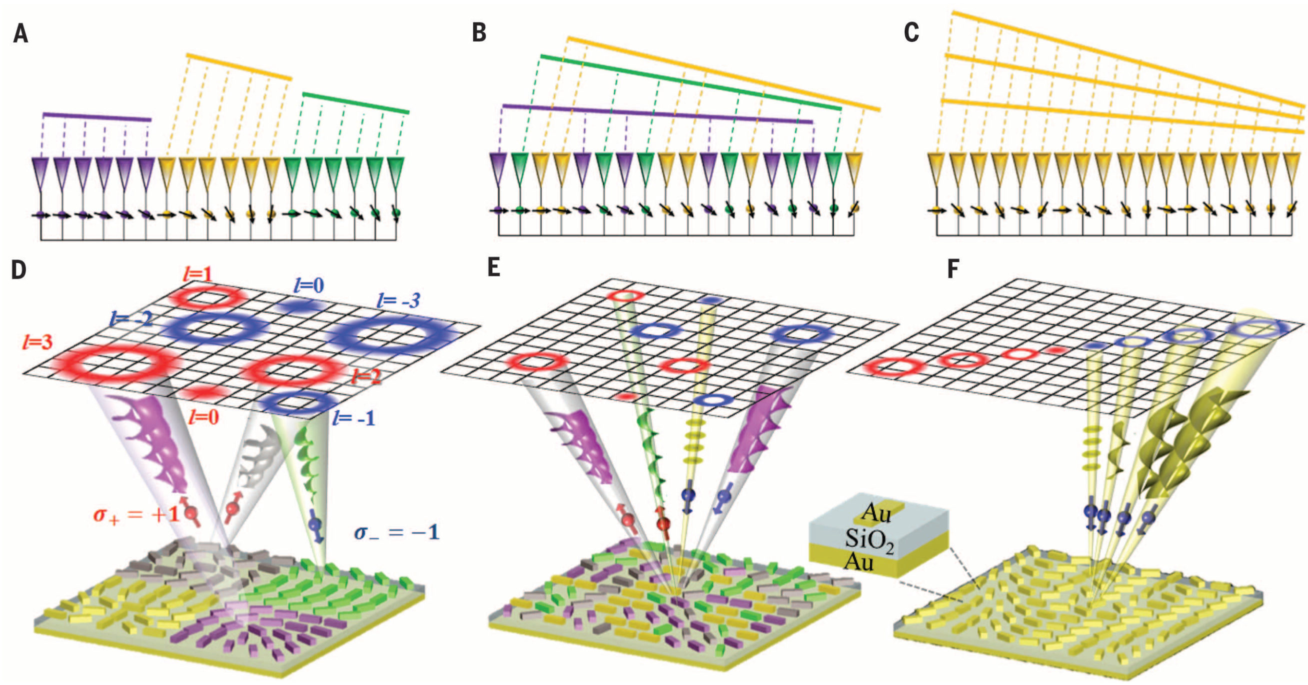

Fig. 1. Schematic of shared-aperture concepts. (**A** to **C**) Segmented (A), interleaved (B), and HR (C) 1D phased arrays. (**D** to **F**) Schematic far-field intensity distribution of wavefronts with positive (red) and negative (blue) helicities emerging from segmented (D), interleaved (E), and HR (F) GPMs composed of gap-plasmon nanoantennas (inset). Here, *l* denotes the topological charge of the spin-dependent OAM wavefronts [for more details, see (*22*)].

spin-orbit interaction phenomenon, a multifunctional GPM, is implemented (Fig. 1).

Photonic GPMs with spatially interleaved phase profiles are designed by the random mixing of optical nanoantenna subarrays, where each subarray provides a different phase function in a spin-dependent manner. This approach makes use of the peculiar ability of random patterns to yield extraordinary information capacity and polarization helicity control via the geometric phase concept. We realized a high-efficiency multifunctional GPM in which the phase and polarization distributions of each wavefront are independently controlled. These GPMs are based on gap-plasmon resonator (GPR) nanoantennas that consist of metal-insulator-metal layers that enable high reflectivity by increasing the coupling between the free wave and the fundamental resonator mode. Moreover, adjustment of the GPR nanoantenna's dimensions enables the design of a high-efficiency half-wave plate (*22*, *23*). For the reflection mode of a single wavefront, we found a diffraction efficiency of ~79%, which is in good agreement with the theory (*10*, *18*, *19*) and the finite-difference time-domain (FDTD) simulation (fig. S1, D to F) (*22*). Then, to design a metasurface generating multiple spin-dependent wavefronts carrying orbital angular momentum (OAM), the GPR nanoantennas were randomly distributed into equal interleaved subarrays. The nanoantennas of each *j*th subarray were oriented according to the relation $2\theta_j(x,y) = k_j x + l_j \varphi$, to obtain momentum redirection $\sigma_\pm k_j$ and topological charge (winding number) $\sigma_\pm l_j$; φ is the azimuthal angle (Fig. 2A). We measured the far-field intensity distribution by illuminating the metasurface with circularly polarized light at a wavelength of 760 nm, and we observed three-by-two spin-dependent OAM wavefronts with the desired topological

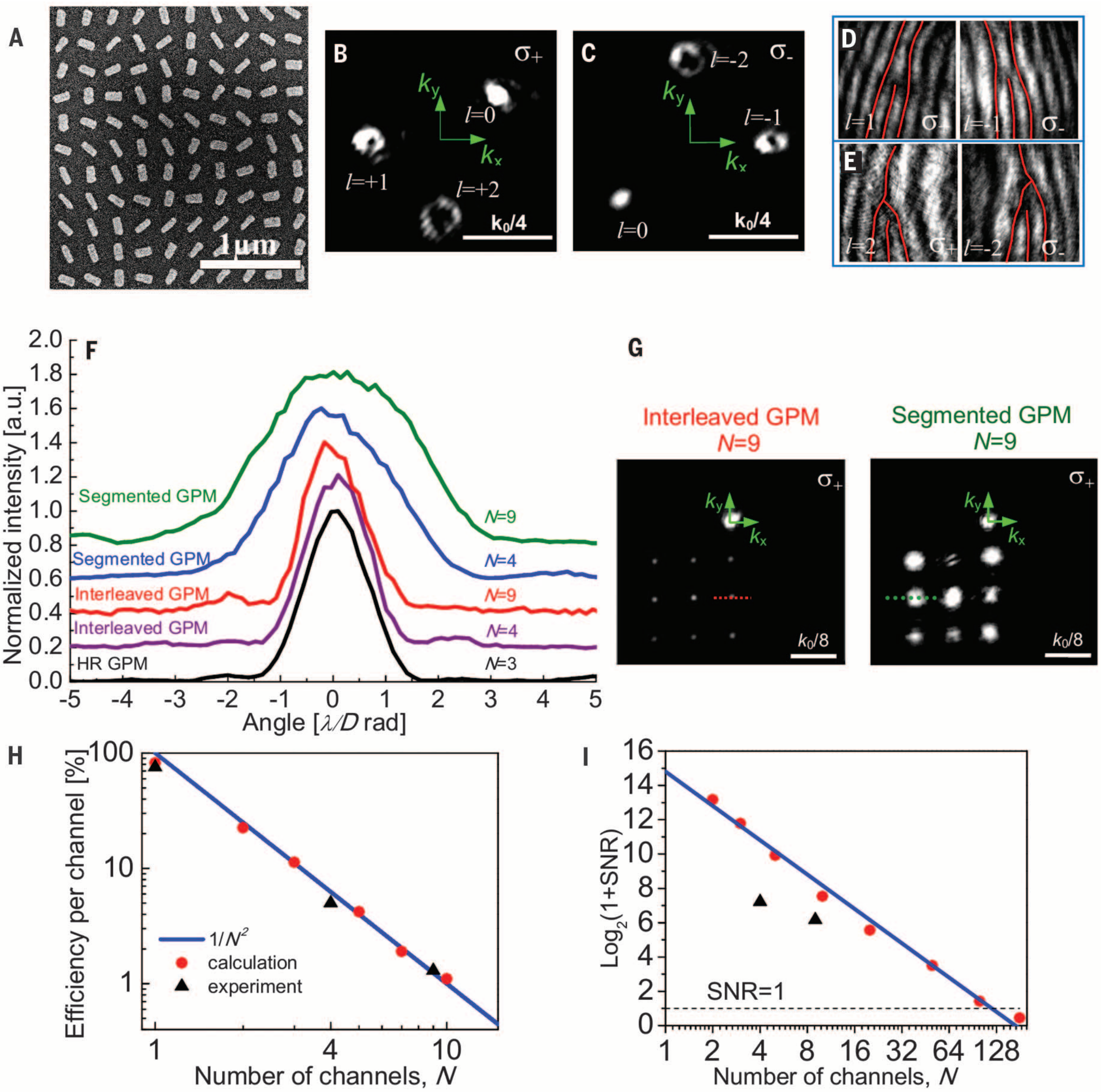

Fig. 2. Multiple wavefront shaping via interleaved GPMs. (**A**) Scanning electron microscope image of a gap-plasmon GPM of aperture D = 50 μm. (**B** and **C**) Measured spin-flip momentum deviation of three wavefronts with different OAMs. $\sigma_\pm$ denotes the incident spin. k_0 is the wave number of the incident beam. (**D** and **E**) Interference pattern of the spin-flipped components with a plane wave, observed from different GPMs generating OAM wavefronts of $l = \pm 1$ (D) and $l = \pm 2$ (E), for σ_- and σ_+ illumination. (**F**) Observed angular width of plane waves emerging from shared-aperture GPMs of different types and numbers of generated channels, corresponding to different colors. a.u., arbitrary units; rad, radians. (**G**) Measured momentum deviations for the interleaved and segmented GPMs, wherein the intensity distributions of nine channels in (F) are presented along the dashed colored lines. (**H** and **I**) Efficiency per channel (H) and number of bits per channel (I). Red dots and black triangles denote the calculation and experiment results, respectively. The blue lines correspond to ~$1/N^2$.

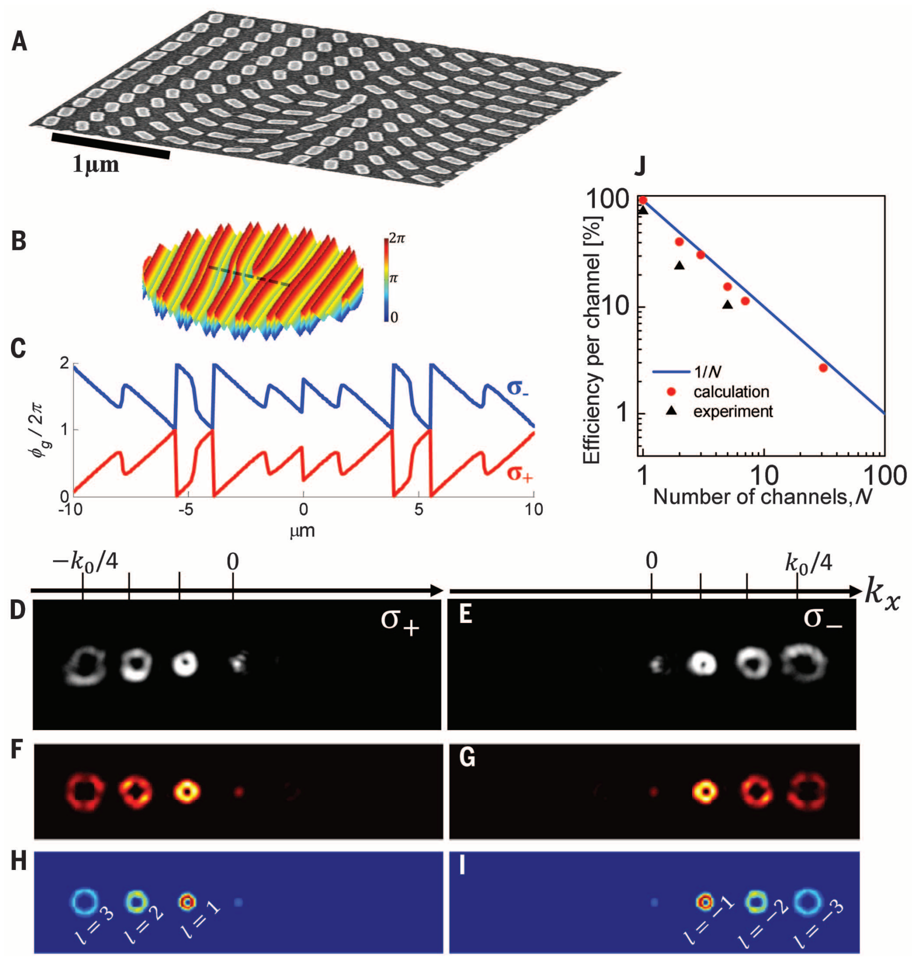

Fig. 3. Spin-dependent asymmetric HR. (**A**) Scanning electron microscope image of the fabricated gap-plasmon HR GPM. (**B**) Geometric phase distribution of the entire HR GPM for σ_+. (**C**) Calculated phase distributions along the 20-μm dashed line in (B) for σ_- (blue) and σ_+ (red). (**D** to **I**) Measured [(D) and (E)], FDTD-simulated [(F) and (G)], and calculated Fourier amplitude [(H) and (I)] spin-dependent HR diffractions of OAM orders, for right (σ_+) and left (σ_-) circular polarization illuminations at a wavelength of λ = 760 nm. The dim zero-order spot arises from an additional harmonic of the "triplicator" phase function and is of negligible efficiency (2%). (**J**) Efficiency per channel. Red dots and black triangles denote the calculation and experiment results, respectively. The blue line corresponds to 1/*N*.

charges of 0, ±1, and ±2 (Fig. 2, B and C), in agreement with FDTD simulation (fig. S2). The corresponding OAMs were verified by measuring the dislocation strength by the interference of the vortex beams with a plane wave (Fig. 2, D and E). An additional peculiar twist in the field of metasurfaces relies on space-variant polarization manipulation, which may encompass a broader class of wavefront shaping. An interleaved GPM enables us to obtain multiple vectorial vortices by coherent superposition of wavefronts with opposite helicities (fig. S6 and movies S1 and S2) (*22*).

We used far-field measurements to experimentally examine the angular resolution characteristics of the interleaved and segmented GPMs. In the segmentation approach, increasing the number of wavefronts (*N*) results in an angular width of $\Delta\Theta \sim \sqrt{N}\cdot\lambda/D$, whereas for the interleaved GPM it is approximately λ/D for an arbitrary *N*, matching the diffraction-limited angular resolution of the shared aperture of size *D* at a wavelength λ (Fig. 2, F and G, and figs. S4 and S5). However, the above analysis does not hold the promise to obtain high information capacity for the interleaved approach, as it is also strongly influenced by the noise originated from channels mixing. The signal-to-noise ratio (SNR) determines the available number of bits per channel as $\log_2(1 + SNR)$ and sets the limit N_c for the channel capacity when *SNR* = 1. To estimate the effect of an incrementally growing number of wavefronts on SNR, the far-field intensity distributions were calculated via Fourier transform (*22*). The calculation shows that the SNR scales as $1/N^2$, leading to a channel capacity limit of $N_c \approx 130$ for the interleaved GPM of *D* = 50 μm (Fig. 2I). Moreover, both the calculations and experiments show that the intensity per channel decreases according to $1/N^2$ (Fig. 2H).

Unlike the interleaved GPM, the harmonic response (HR) metasurface is not limited by the intensity scaling of $1/N^2$. The HR concept relies on different optimization methods, iterative and analytic, and has been implemented in a variety of realms such as holography, communication, and radar (*24–26*). To obtain spin-dependent asymmetric harmonic diffraction orders, we incorporated the HR and geometric phase concepts. The geometric phase function can be expanded to spin-dependent OAM harmonic orders $A_m\exp[im\sigma_\pm(kx+\varphi)]$ (where A_m is the amplitude of *m*th order and *i* is the square root of −1), where $\sigma_\pm mk$ is the momentum redirection of *m*th order. The phase function can be optimized to achieve identical intensities $|A_m|^2 \approx 1/(b-a+1)$ for selected asymmetric orders $a < m < b$ with maximal optical efficiency. We adopted an optimized analytic solution [the "triplicator" (*25*)] to realize a GPM (Fig. 3, A to C) providing three spin-dependent asymmetric OAM harmonic orders (*22*). The GPM was illuminated with right and left circularly polarized light, and the spin-dependent diffraction pattern consisting of multiple OAM harmonic orders of $l_\pm = \sigma_\pm, 2\sigma_\pm, 3\sigma_\pm$ corresponding to *m* = 1, 2, 3 was observed (Fig. 3, D and E). The diffraction patterns were verified by the spin-dependent FDTD simulation (Fig. 3, F and G) and by calculating Fourier amplitudes (Fig. 3, H and I). The efficiencies of each order were measured to be $|A_m|^2 \cong 0.21$ with uniformity of ±0.01, leading to a total efficiency of ~63%, in accordance with the intensity scaling of $1/N$ (Fig. 3J) (*22*). Furthermore, we experimentally confirmed that the HR approach is manifested by diffraction-limited angular resolution of the shared aperture (Fig. 2F, and fig. S7, B and F). In light of the above, the HR concept constitutes a suitable platform to realize a well–angular resolved multibeam possessing negligible noise and thus able to provide high information capacity, whereas the interleaving approach suffers from the speckle noise and is hindered by capacity reduction. On the other hand, the latter approach offers high flexibility in multifunctional wavefront generation, whereas with the HR concept, harmonic sequence restricts this flexibility. Moreover, the

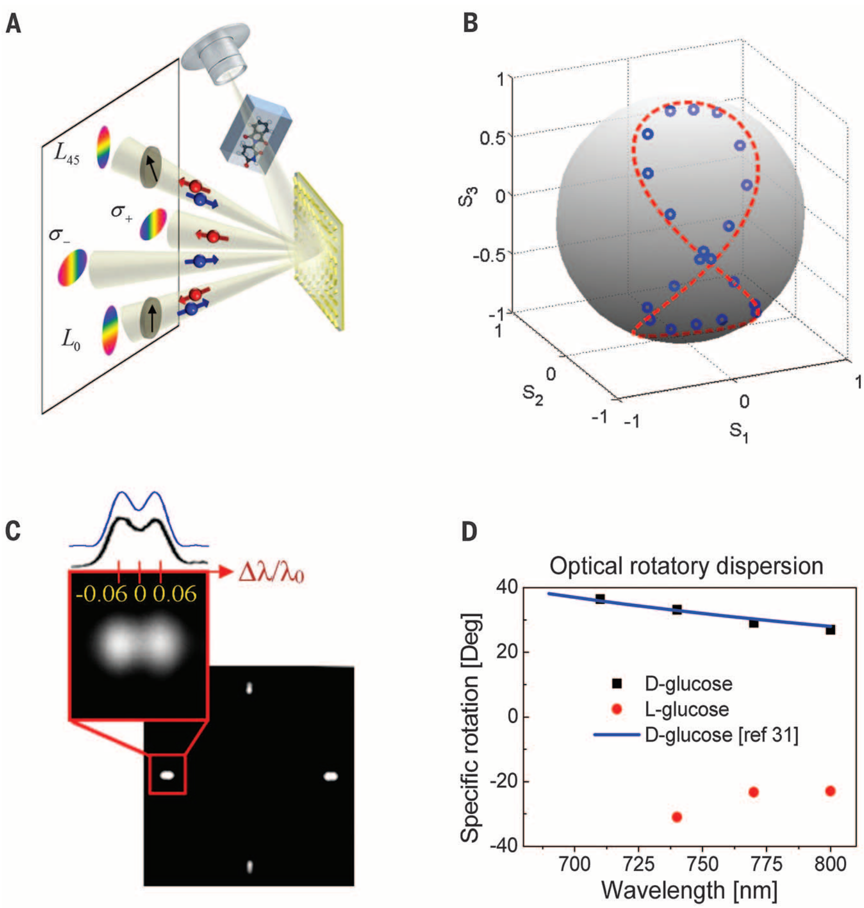

Fig. 4. Spectropolarimeter metasurface. (**A**) Schematic setup of the spectropolarimeter. The SPM is illuminated by a continuum light passing through a cuvette with chemical solvent, then four beams of intensities I_{σ_+}, I_{σ_-}, I_{L45}, and I_{L0} are reflected toward a charge-coupled device camera. (**B**) Predicted (red dashed curve) and measured (blue circles) polarization states, obtained by a polarization-state generator (a linear polarizer followed by a rotated quarter-wave plate), depicted on a Poincaré sphere. (**C**) Measured far-field intensities for elliptical polarization at two spectral lines (with wavelengths of 740 and 780 nm) and (inset) the corresponding resolving power (black line) and calculation (blue line) of the 50-μm diameter SPM. (**D**) ORD for the specific rotations of D- and L-glucose. Black squares and red circles represent the measured ORD of D- and L-glucose, respectively. The blue line depicts the dispersion acquired from (*31*).

reported spin-controlled multifunctional metasurfaces based on shared-aperture approaches are studied in terms of information capacity by means of Wigner phase-space distribution to establish a link between the Shannon entropy and the capacity of photonic system (fig. S8) (*22*).

Spectropolarimetry is an application for the simultaneous measurement of the spectrum and polarization state of light and is widely used to characterize chemical compounds. Implementing spectropolarimetric devices with metasurfaces opens new avenues for on-chip detection. Recently, on-chip chiroptical spectroscopy (*27*) was presented, measuring the differential absorption between left- and right-circular polarizations. The device used in this experiment is unable to provide full polarization analysis. Furthermore, it has been shown that a metasurface allows for the simultaneous determination of the Stokes parameters (i.e., the polarization state of light) (*28*, *29*) without consideration of the spectral analysis. Here we propose a simple, fast, and compact technique, based on an interleaved GPM, that can simultaneously characterize the polarization state and spectrum of a wave transmitted through a semitransparent object. The spectropolarimeter metasurface (SPM) is composed of three interleaved linear phase profiles ($\phi_g^{(1)} = \sigma_\pm k_x x; \phi_g^{(2)} = \sigma_\pm k_y y; \phi_g^{(3)} = \sigma \pm k_y y$) associated with different nanoantenna subarrays. When a probe beam with an arbitrary polarization state impinges on the SPM, two beams of intensities $I_{\sigma_\pm}$, consisting of opposite helicity states, and two additional beams emerge. The latter have identical polarizations, conjugate with respect to the incident beam, and being projected onto linear polarizers at 0° and 45° determines the linearly polarized components I_{L0} and I_{L45}, respectively (Fig. 4A). The Stokes parameters of the probed beam are then calculated by the expressions (*28*) $S_0 = 2(I_{\sigma_+} + I_{\sigma_-})/\eta$, $S_1 = 2I_{L0}/\eta - S_0$, $S_2 = 2I_{L45}/\eta - S_0$, and $S_3 = 2(I_{\sigma_+} - I_{\sigma_-})/\eta$, where the coefficient (η) is determined by a calibration experiment (fig. S9). The SPM of 50-μm diameter was normally illuminated by a supercontinuum light source, passing through the acousto-optic modulator, which enables the tenability of various wavelengths. Figure 4B shows the measured and calculated Stokes parameters on a Poincaré sphere for an analyzed beam impinging the SPM at a wavelength of 760 nm with different polarizations, obtained by a polarization-state generator (linear polarizer followed by a rotated quarter-wave plate). The spectral resolving power is defined according to the Rayleigh criterion as $\lambda/\Delta\lambda = q/M_{x,y}{}^2$, where $M_{x,y}{}^2$ is the beam quality parameter in each direction (x, y) and q is the number of phase-modulation periods (*30*). The resolving power of the SPM was measured and found to be $\lambda/\Delta\lambda \cong 13$ (Fig. 4C). The obtained value is in good agreement with the calculated resolving power for SPM with $q \cong 17$ periods and a laser beam quality of $M_{x,y}{}^2 = 1.3$. We measured the optical rotatory dispersion (ORD) for the specific rotations of D-glucose (chiral molecule) and its enantiomer L-glucose that were dissolved in water with predetermined concentrations (Fig. 4D) (*22*). The ORD of D-glucose shows a good agreement with the values found in the literature (*31*), whereas the L-glucose ORD is manifested by the opposite behavior as expected. We achieved real-time on-chip spectropolarimetry by exploiting the interleaved GPM. The reported alliance of the spin-enabled geometric phase and shared-aperture concepts sheds light on the multifunctional wavefront manipulation in a spin-dependent manner. The introduced asymmetric HR and interleaved GPMs constitute suitable candidates to realize on-demand multifunctional on-chip photonics.

REFERENCES AND NOTES

1. D. M. Pozar, S. D. Targonski, *IEEE Trans. Antenn. Propag.* **49**, 150–157 (2001).
2. R. L. Haupt, *IEEE Trans. Antenn. Propag.* **53**, 2858–2864 (2005).
3. A. M. Sayeed, V. Raghavan, *IEEE J. Sel. Top. Signal Process.* **1**, 156–166 (2007).
4. I. E. Lager, C. Trampuz, M. Simeoni, L. P. Ligthart, *IEEE Trans. Antenn. Propag.* **57**, 2486–2490 (2009).
5. A. Papakostas *et al.*, *Phys. Rev. Lett.* **90**, 107404 (2003).
6. X. Yin, Z. Ye, J. Rho, Y. Wang, X. Zhang, *Science* **339**, 1405–1407 (2013).

7. A. Pors, O. Albrektsen, I. P. Radko, S. I. Bozhevolnyi, *Sci. Rep.* **3**, 2155 (2013).
8. A. V. Kildishev, A. Boltasseva, V. M. Shalaev, *Science* **339**, 1232009 (2013).
9. N. Yu, F. Capasso, *Nat. Mater.* **13**, 139–150 (2014).
10. D. Lin, P. Fan, E. Hasman, M. L. Brongersma, *Science* **345**, 298–302 (2014).
11. M. G. Nielsen, D. K. Gramotnev, A. Pors, O. Albrektsen, S. I. Bozhevolnyi, *Opt. Express* **19**, 19310–19322 (2011).
12. D. Dregely *et al.*, *Nat. Commun.* **5**, 4354 (2014).
13. J. Sun *et al.*, *Nano Lett.* **14**, 2726–2729 (2014).
14. H.-S. Ee, J.-H. Kang, M. L. Brongersma, M.-K. Seo, *Nano Lett.* **15**, 1759–1765 (2015).
15. K. E. Chong *et al.*, *Nano Lett.* **15**, 5369–5374 (2015).
16. Z. Bomzon, V. Kleiner, E. Hasman, *Opt. Lett.* **26**, 1424–1426 (2001).
17. Z. Bomzon, G. Biener, V. Kleiner, E. Hasman, *Opt. Lett.* **27**, 1141–1143 (2002).
18. G. Biener, A. Niv, V. Kleiner, E. Hasman, *Opt. Lett.* **27**, 1875–1877 (2002).
19. A. Niv, G. Biener, V. Kleiner, E. Hasman, *Opt. Express* **14**, 4208–4220 (2006).
20. N. Dahan, Y. Gorodetski, K. Frischwasser, V. Kleiner, E. Hasman, *Phys. Rev. Lett.* **105**, 136402 (2010).
21. K. Y. Bliokh, F. J. Rodríguez-Fortuño, F. Nori, A. V. Zayats, *Nat. Photonics* **9**, 796–808 (2015).
22. Full details can be found in the supplementary materials on *Science* Online.
23. A. Pors, M. G. Nielsen, S. I. Bozhevolnyi, *Opt. Lett.* **38**, 513–515 (2013).
24. H. Dammann, K. Görtler, *Opt. Commun.* **3**, 312–315 (1971).
25. F. Gori *et al.*, *Opt. Commun.* **157**, 13–16 (1998).
26. J. Albero *et al.*, *Appl. Opt.* **52**, 3637–3644 (2013).
27. A. Shaltout, J. Liu, A. Kildishev, V. Shalaev, *Optica* **2**, 860–863 (2015).
28. Y. Gorodetski, G. Biener, A. Niv, V. Kleiner, E. Hasman, *Opt. Lett.* **30**, 2245–2247 (2005).
29. A. Pors, M. G. Nielsen, S. I. Bozhevolnyi, *Optica* **2**, 716–723 (2015).
30. N. Davidson, L. Khaykovich, E. Hasman, *Opt. Lett.* **24**, 1835–1837 (1999).
31. A. Penzkofer, *J. Anal. Sci. Methods Instrum.* **3**, 234–239 (2013).

ACKNOWLEDGMENTS

This research was supported by the United States–Israel Binational Science Foundation, the Israel Science Foundation, the Israel Nanotechnology Focal Technology Area on Nanophotonics for Detection, and KLA-Tencor.

SUPPLEMENTARY MATERIALS

www.sciencemag.org/content/352/6290/1202/suppl/DC1
Supplementary Text
Figs. S1 to S9
References (*32*–*44*)
Movies S1 and S2

28 January 2016; accepted 8 April 2016
Published online 21 April 2016
10.1126/science.aaf3417

MAGNETISM

Orbital-exchange and fractional quantum number excitations in an f-electron metal, Yb_2Pt_2Pb

L. S. Wu,[1,2,3] W. J. Gannon,[1,2,4] I. A. Zaliznyak,[2*] A. M. Tsvelik,[2] M. Brockmann,[5,6] J.-S. Caux,[6] M. S. Kim,[2] Y. Qiu,[7] J. R. D. Copley,[7] G. Ehlers,[3] A. Podlesnyak,[3] M. C. Aronson[1,2,4]

Exotic quantum states and fractionalized magnetic excitations, such as spinons in one-dimensional chains, are generally expected to occur in 3d transition metal systems with spin 1/2. Our neutron-scattering experiments on the 4f-electron metal Yb_2Pt_2Pb overturn this conventional wisdom. We observe broad magnetic continuum dispersing in only one direction, which indicates that the underlying elementary excitations are spinons carrying fractional spin-1/2. These spinons are the emergent quantum dynamics of the anisotropic, orbital-dominated Yb moments. Owing to their unusual origin, only longitudinal spin fluctuations are measurable, whereas the transverse excitations such as spin waves are virtually invisible to magnetic neutron scattering. The proliferation of these orbital spinons strips the electrons of their orbital identity, resulting in charge-orbital separation.

It is generally believed that fractional quantum excitations such as spinons in one-dimensional (1D) spin chains proliferate and govern magnetism only in systems with small and isotropic atomic magnetic moments, such as spin-1/2 Cu^{2+}. In contrast, large and anisotropic orbital-dominated moments, such as those produced by strong spin-orbit coupling in the rare earths, are considered to be classical, becoming static as temperature $T \to 0$ because the conventional Heisenberg-Dirac exchange interaction (*1*, *2*) cannot reverse their directions. Here we present the results of neutron-scattering measurements on the 3D compound Yb_2Pt_2Pb that profoundly challenge this conventional wisdom.

The unusual properties of Yb_2Pt_2Pb derive in part from its crystal structure (Fig. 1, A and B), where the Yb^{3+} ions form ladders along the *c* axis, separated by Pt and Pb; the rungs of the ladders (dashed lines in Fig. 1A) lie on the orthogonal bonds of the Shastry-Sutherland lattice (SSL) (*3*) in the *ab* planes. Equally important is the strong spin-orbit coupling, which combines spin and orbital degrees of freedom into a large, $J = 7/2$ Yb moment. The absence of a Kondo effect indicates minimal coupling of Yb to the conduction electrons of this excellent metal (*4*, *5*). A point-charge model (*6*) indicates that the crystal electric field (CEF) lifts the eightfold degeneracy of the Yb^{3+} moments, producing a Kramers doublet ground state that is a nearly pure state of the total angular momentum, J, $|J, m_J\rangle = |7/2, \pm 7/2\rangle$. The estimated anisotropy of the Landé g factor is in good agreement with that of the measured magnetization, $g_{||}/g_{\perp} = 7.5(4)$ (*4*–*7*), implying strong Ising anisotropy in Yb_2Pt_2Pb, which confines the individual Yb moments to two orthogonal sublattices in the *ab* plane.

The quantum states of the $|\pm 7/2\rangle$ Ising doublet are the superpositions of its "up" and "down" components, $\alpha_{\uparrow}|7/2\rangle + \alpha_{\downarrow}|-7/2\rangle$, and therefore the doublet can be viewed as an effective quantum spin-1/2. However, familiar interactions like the Zeeman, Heisenberg-Dirac exchange, and dipole interactions that are bilinear in J can only change the total angular momentum quantum number by $\Delta m_J = \pm 1$; they have no matrix elements that would allow transitions between the moment-reversed states of the ground state wave function. Only multiple virtual processes involving excited states could reverse individual Yb moments, but these processes are expected to be very weak because the ground and first excited states are separated by as much as 25 meV, according to specific heat (*4*) and inelastic neutron-scattering measurements (*6*). This would suggest that Yb_2Pt_2Pb would display only static, classical Ising behavior, but our data are not consistent with this picture.

Here we report neutron-scattering experiments on Yb_2Pt_2Pb that reveal a continuum of low-energy quantum excitations that display the distinctive spinon dispersion along the *c* axis (Fig. 2A), typical of the $S = 1/2$ Heisenberg-Ising XXZ spin Hamiltonian (*8*),

$$H = \mathrm{J}\sum_{n}(S_n^x S_{n+1}^x + S_n^y S_{n+1}^y + \Delta S_n^z S_{n+1}^z) \quad (1)$$

where J is the Heisenberg spin-exchange coupling and Δ is its anisotropy. This observation provides definitive evidence that the Yb moments in Yb_2Pt_2Pb behave as quantum-mechanical spins-1/2 (*9*). The spinon spectrum $M(\boldsymbol{Q}, E)$ is fully gapped, but the gap is much smaller than the excitation bandwidth, indicating only moderate Ising anisotropy, $\Delta \gtrsim 1$. The lack of any wave

[1]Department of Physics and Astronomy, Stony Brook University, Stony Brook, NY 11794, USA. [2]Condensed Matter Physics and Materials Science Division, Brookhaven National Laboratory, Upton, NY 11973, USA. [3]Quantum Condensed Matter Division, Oak Ridge National Laboratory, Oak Ridge, TN 37831, USA. [4]Department of Physics and Astronomy, Texas A&M University, College Station, TX 77843, USA. [5]Max Planck Institute for the Physics of Complex Systems, Nöthnitzer Strasse 38, 01187 Dresden, Germany. [6]Institute for Theoretical Physics, University of Amsterdam, Science Park 904, 1098 XH Amsterdam, Netherlands. [7]NIST Center for Neutron Research, National Institute of Standards and Technology, Gaithersburg, MD 20899, USA.
*Corresponding author. Email: zaliznyak@bnl.gov

Photonic spin-controlled multifunctional shared-aperture antenna array
Elhanan Maguid, Igor Yulevich, Dekel Veksler, Vladimir Kleiner, Mark L. Brongersma and Erez Hasman (April 21, 2016)
Science **352** (6290), 1202-1206. [doi: 10.1126/science.aaf3417]
originally published online April 21, 2016

Editor's Summary

Multifunction planar optics

Specially designed two-dimensional (2D) arrays of nanometer-scale metallic antennas, or metasurfaces, may allow bulky optical components to be shrunk down to a planar device structure. Khorasaninejad *et al.* show that arrays of nanoscale fins of TiO can function as high-end optical lenses. At just a fraction of the size of optical objectives, such planar devices could turn your phone camera or your contact lens into a compound microscope. Maguid *et al.* interleaved sparse 2D arrays of metal antennas to get multifunctional behavior from the one planar device structure (see the Perspective by Litchinitser). The enhanced functionality of such designed metasurfaces could be used in sensing applications or to increase the communication capacity of nanophotonic networks.

Science, this issue pp. 1190 and 1202; see also p. 1177